

# Double-functioned metalens inspired by compound eyes for naked-eye 3D display with high efficiency, high resolution, and large viewing range

Jian Zhu (朱建)<sup>1</sup>, Qinyue Sun (孙秦悦)<sup>2</sup>, Zhenhuan Tian (田振寰)<sup>2\*</sup>, Xuzheng Wang (王旭正)<sup>2</sup>, Feng Li (李峰)<sup>2</sup>, and Feng Yun (云峰)<sup>2\*\*</sup>

<sup>1</sup>School of Mechanical Engineering, Xi'an Jiaotong University, Xi'an 710049, China

<sup>2</sup>Shaanxi Provincial Key Laboratory of Photonics & Information Technology, Xi'an Jiaotong University, Xi'an 710049, China

\*Corresponding author: [tianzhenhuan@xjtu.edu.cn](mailto:tianzhenhuan@xjtu.edu.cn)

\*\*Corresponding author: [fyun2010@xjtu.edu.cn](mailto:fyun2010@xjtu.edu.cn)

Received August 25, 2024 | Accepted January 23, 2025 | Posted Online May 30, 2025

Micro-LED is one of the most promising technologies for naked-eye 3D display. However, due to challenges related to efficiency, resolution, viewing range, and structure integration, the 3D micro-LED display is still at the conceptual stage. In this work, we introduce a double-functioned metalens composed of highly symmetric unit cells into the 3D micro-LED system. The nonpolarized spotlight generated by the micro-LED is collimated and deflected through the designed metalens. Inspired by the compound eyes, metalens modules with varying deflection angles are spliced and penetrated together, enabling a wide viewing angle without sacrificing resolution. Additionally, the viewing position can be dynamically adjusted using adjustable subpixels. The results demonstrate that the proposed metalens and its optical system can reach a viewing angle ranging from  $-41.5^\circ$  to  $41.5^\circ$  and an adjustable optimum viewing distance from 25 to 75 cm. The deflection efficiency exceeds 80%, with a resolution of 910 PPI (pixels per inch). Our design shows great potential for naked-eye 3D display.

**Keywords:** 3D display; metalens; viewing angle; high resolution.

**DOI:** [10.3788/COL202523.063604](https://doi.org/10.3788/COL202523.063604)

## 1. Introduction

With the advancement of science and technology, the transition from two-dimensional (2D) to three-dimensional (3D) display technology has become an inevitable trend. Naked-eye 3D display, as one of the most prominent 3D technologies, enables viewers to experience an exceptionally vivid visual experience without wearing a pair of glasses. The naked-eye display system consists of a 2D display panel with a light-controlling component, such as a parallax barrier and a lenticular lens<sup>[1-3]</sup>. Among various 2D display technologies, micro-LED offers significant advantages in high contrast, low power consumption, and high response frequency<sup>[4-6]</sup>, making it an ideal technology for naked-eye displays<sup>[7-9]</sup>. However, the 3D micro-LED display is still at the conceptual stage, limited by its intrinsic emission properties of large divergence angles and noncoherence. Engineered micro-LED systems with controllable luminescence distribution and direction should advance the naked-eye 3D micro-LED display.

Normally, micro-LED shows a Lambertian emission with a wide divergence angle higher than  $\pm 60^\circ$ <sup>[10]</sup>. Engineered optical

components, such as hemispherical lenses, microgratings, and photonic crystals, are required to collimate the emitted light, resulting in complex systems, bulky volumes, and low efficiencies<sup>[11-14]</sup>. Resonant cavities incorporated with distributed Bragg reflectors (DBRs) demonstrate a small beam divergence ( $9^\circ$ ) while maintaining a size comparable to micro-LED<sup>[15]</sup>. Additionally, a resonant cavity can also be used to increase the LED's spatial coherence. However, the emission direction is sensitive to the cavity length and emission wavelength, making it highly angle-dependent<sup>[16]</sup>. Metasurfaces, composed of periodic similar structures, are capable of precise light manipulation. Therefore, Kuznetsov proposed an optical system that combined the resonant cavity with a specially designed metasurface to obtain controllable photoluminescence direction<sup>[17]</sup>. Furthermore, some research has developed optical systems that demonstrate unidirectional emission with controllable full width at half-maximum (FWHM) at arbitrary angles (for example,  $10^\circ$ ,  $20^\circ$ , and  $30^\circ$ )<sup>[18]</sup>. However, because of the utilization of the cavity structure, the luminous efficiency of the resonant cavity light-emitting diode (RCLED) is unsatisfying (8%), and the

FWHM of the deflected light is still too large, resulting in obvious cross talk<sup>[17,19]</sup>. Additionally, the cavity structure also increases the difficulty in fabrication and integration with the existing display panel. Therefore, achieving efficient collimated and directional light without the use of a resonant cavity is the key challenge.

Despite the issues arising from the instinct properties of micro-LED, 3D optical systems face the problems of small viewing angles and a limited observation range<sup>[20]</sup>. To achieve a large viewing angle, the current approach involves using several subpixels to achieve a multiview, which sacrifices resolution<sup>[21]</sup>. Additionally, the optimum viewing distance is fixed<sup>[22]</sup>. However, the observation position may vary greatly according to different usage scenarios. Therefore, it is necessary to find a way to dynamically control the deflective direction and the viewing distance without sacrificing its efficiency and resolution.

To solve the issues of efficiency, viewing range, resolution, and structure integration, we present what we believe is a novel approach utilizing a metalens with dual functionality in collimation and deflection. Unlike conventional techniques, the metalens is independent from the light source by avoiding the resonance cavity, resulting in a simplification of the fabrication process and increasing the probability of integration with the existing 2D display. Inspired by the compound eyes, the metalens integrated with one subpixel can achieve multideflection, contributing to a large viewing angle without sacrificing resolution. Additionally, the viewing positions can be dynamically adjusted by adjusting the images that the subpixels transmit. Using the finite-difference time-domain (FDTD) method, the performance of the micro-LED integrated with the metalens is thoroughly analyzed. The simulation results demonstrate that the optical system can achieve a viewing angle of  $-41.5^\circ$  to  $41.5^\circ$  and allows for dynamically adjustable viewing positions, with a deflection efficiency exceeding 80%. Theoretically, our design enables a feasible control of viewing position and excellent performance in luminous efficiency, making it suitable for a highly integrated micro-LED 3D display.

## 2. Design and Principle

### 2.1. Design principle of metalens-based naked-eye 3D display

The naked-eye 3D display proposed in this work consists of a 2D display panel and an “optical layer” with a metastructure. Different from the lenticular-based 3D display, which directs the light of neighboring sub-pixels into different directions by adding cylindrical lens, the metalens-based 3D display can deflect the light generated by the individual subpixel into different directions, as shown in Figs. 1(a) and 1(b). Therefore, the metalens-based 3D display offers higher resolution. In an eight-view monochrome 3D display, for example, the original eight subpixels of 2D display can only support a single pixel for lenticular-based 3D display. However, a pair of subpixels from 2D display contributes to one pixel for metalens-based

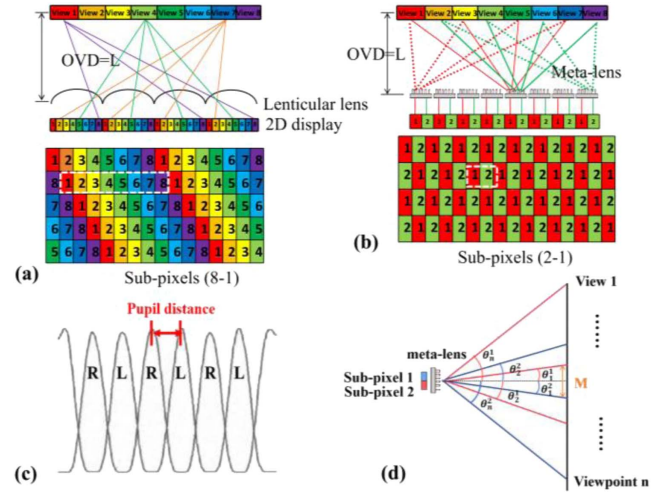


Fig. 1. Schematics of (a) 3D display system based on lenticular lens, (b) 3D display based on a metalens, (c) illuminance distribution varied with the viewing positions for subpixel 1 and subpixel 2, and (d) calculation method of the deflection angle for subpixels.

3D display, with subpixel 1 for the left-eye image and subpixel 2 for the right-eye image. The illuminance distribution varied with the viewing position is illustrated in Fig. 1(c). The focal points generated by subpixel 1 and subpixel 2 alternately exist in space. The distance between the peaks of the focal points at the optimum viewing distance (OVD) should fix the pupil distance<sup>[22]</sup>.

To ensure that the distance of adjacent peaks meets the pupil distance, the deflection angle of the light generated from subpixels needs to be carefully controlled. Figure 1(d) demonstrates the calculation method of the deflection angle for subpixel 1 and subpixel 2 through a metalens,

$$\begin{cases} \theta_n^1 = (-1)^{(n-1)} \arctan[M \cdot (2n-1)/2L] \\ \theta_n^2 = (-1)^n \arctan[M \cdot (2n-1)/2L] \end{cases}, \quad (1)$$

where  $M$  is the pupil distance,  $L = \text{OVD}$  is the distance between the display and the optimized observation screen,  $\theta_n^1$  is the deflection angle of subpixel 1 through the metalens, and  $\theta_n^2$  is the deflection angle of subpixel 2 through the metalens. Therefore, the designed metalens should have a function of multiple deflections. In an eight-view display, for example, the metalens designed for subpixel 1 requires angular deflection in  $-41.5^\circ$ ,  $-22^\circ$ ,  $8^\circ$ , and  $33.8^\circ$ ; while for subpixel 2, the deflection angles are  $-33.8^\circ$ ,  $-8^\circ$ ,  $22^\circ$ , and  $41.5^\circ$  with a given  $L = 25$  cm and  $M = 65$  mm.

### 2.2. Design of double-functioned metalens and bionic compound eye metasurface for multiview display

The 2D display panel consists of numerous independently driven LED chips. Each LED chip generates uncollimated and noncoherent light, acting as a subpixel. Therefore, the metalens not only needs to show a function of multideflection but

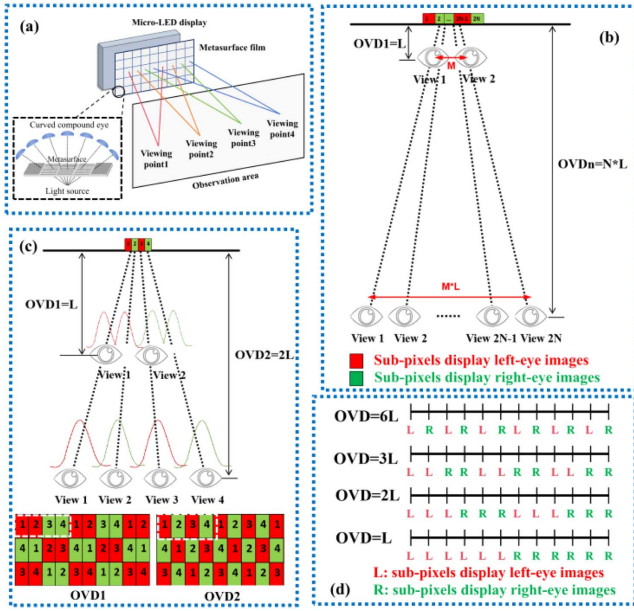


Fig. 2. (a) Schematic of double-functioned metalens and bionic compound eye metasurface for multiview display, and image designs for (b) optical system with  $2N$  subpixels, (c) optical system with four subpixels, and (d) optical system with 12 subpixels.

also needs to solve the problem of collimation. Aiming at the double function, the phase distribution of the metalens can be calculated by combining the deflection with the collimation,

$$\Phi = \Phi_1 + \Phi_2 = -\frac{2\pi}{\lambda} \sin \theta \cdot x - \frac{2\pi}{\lambda} \left( \sqrt{x^2 + f^2} - f \right), \quad (2)$$

where  $x$  is the coordinate position of the unit cell distribution,  $\lambda$  is the working wavelength in the free space, which is 532 nm,  $f$  is the focal length, and  $\theta$  is the deflection angle.

Further, to ensure a viewing angle larger than  $40^\circ$ , we innovatively introduce a bionic compound eye metasurface, which consists of several double-functioned metalens modules, as illustrated in Fig. 2(a). These metalens modules with different deflection angles are spliced and penetrated together, resulting in multiple deflections of the original subpixel.

### 2.3. Design methodology of metalens for dynamically controlled viewing distance

The designed metalens with a fixed deflection angle can only ensure a well-performed 3D emission at a specific viewing distance. A slight deviation of the observation point will result in serious cross talk and image shift. The acceptable offset of the eye pupil distance is generally within 4 mm, and the tolerance of the viewing distance is less than 6%<sup>[22]</sup>. However, the observation position may vary greatly according to the needs of different situations, e.g., mobile phones, computers, and televisions, varying from 20 to 100 cm.

In order to extend its application scope,  $2N$  subpixels in the 2D display are combined to form one pixel in the 3D display, as

shown in Fig. 2(b). Half of the subpixels transmit images for the left eye, and the other half are for the right eye. The viewing distance can be dynamically controlled by adjusting the images transmitted by each subpixel. For an optical system with  $2N$  subpixels, the OVD can be varied from  $L$  to  $N \cdot L$ . If  $N$  can be decomposed into the product of several prime numbers,  $N = n_1 \cdot n_2 \cdots n_x$ , where  $n_1 \cdot n_2 \cdots n_x$  are all prime numbers. Then, any composite number  $N_x$  composed of  $n_1 \cdot n_2 \cdots n_x$  can be used to support an OVD.

Figure 2(c) shows an example of an optical system with four subpixels, which can support two optimum viewing distances. If subpixels 1 and 2 show images for the left eye and subpixels 3 and 4 display images for the right eye, the OVD is  $L$ ; if subpixels 1, 2, 3, and 4 are alternately arranged for left and right eyes, the OVD is  $2L$ . The deflection angles of subpixels 1 and 3 can also be calculated using Eq. (1). The additional subpixels 2 and 4 can be calculated using Eq. (3),

$$\theta = \pm \arctan[M \cdot (n - 1)/2L]. \quad (3)$$

Figure 2(d) demonstrates the design of an optical system with 12 subpixels, where  $N = 1 \cdot 2 \cdot 3$ . Therefore, the viewing distance can be set to  $L$ ,  $2L$ ,  $3L$ , and  $6L$ . When the OVD =  $2L$ , the subpixels are alternately arranged for the left and right eyes in groups of three. When the observation distance is  $3L$ , two adjacent subpixels are in one group. When the observation distance is  $6L$ , adjacent subpixels are driven separately for different eyes. The deflection angles of subpixels 1 and 6 can also be calculated using Eq. (1). The additional subpixels can be determined using the equation below,

$$\begin{cases} \theta = \pm \arctan[(3M \cdot n - 5M)/6L] \\ \theta = \pm \arctan[(3M \cdot n - 7M)/6L] \end{cases} \quad (4)$$

## 3. Results and Discussion

### 3.1. Double-functioned metalens with a specific deflection angle

We use the FDTD method to simulate the deflection characteristics of the designed metalens, accompanied by a micro-LED. The unit structure of the metalens consists of a cylindrical structure made of GaN, with a refractive index of 2.4 at  $\lambda = 532$  nm, as demonstrated in Fig. 3(a). The compensation phase and transmission efficiency can be adjusted by varying the radius ( $R$ ), height ( $H$ ), and period of the cylinder. As an artificial subwavelength structure, the metasurface requires a period smaller than the wavelength of the incident light<sup>[23]</sup>. Thus, the designed unit structure is set with period parameters of 400 nm. Additionally, to suppress the diffraction effects, the diameter of the nanorods should be less than half of the operating wavelength<sup>[24]</sup>. Therefore, the radius parameter range is set from 40 to 150 nm. Considering the limitations of fabrication technology, the height parameter is set from 100 to 800 nm. The simulated phase and transmission maps are shown in Figs. 3(c) and 3(d). The results demonstrate that the phase can cover  $2\pi$  with varied parameters

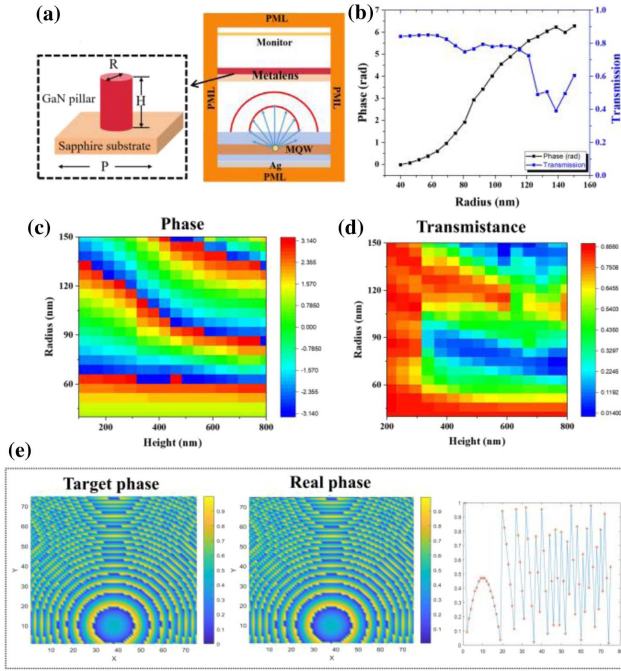


**Fig. 3.** (a) Schematic diagram of the metalens integrated with micro-LED for FDTD simulation; (b) numerical calculations for the transmittance and phase shift as a function of the radius; (c) phase varying with radius and height; (d) transmittance varying with radius and height; (e) comparison of the target phase and the real phase.

for the designed unit, and the transmissions of most structures exceed 0.8 with a height of 600 nm, as shown in Fig. 3(b).

By utilizing the selected structures, the double-functional metalens for an eight-view display can be designed based on Eq. (2), where the deflection angle can be calculated by Eq. (1). The calculated deflection angles are listed in Table 1. To find the specific unit cells fitting the equation, particle swarm optimization (PSO) is employed. Figure 3(e) illustrates the target and real phase of the designed metalens with a deflection angle of 8°. The results demonstrate that the phase distribution of the designed metalens matches well with the theoretical values.

To investigate the deflection performance, the simulation model of the integrated metalens with micro-LED sources is further developed, as shown in Fig. 3(a). The structure consists of a 200 nm metal reflection layer (Ag) at the bottom, followed by a 200 nm P-GaN layer, a 200 nm multiple quantum well (MQW) layer, and a 3 μm N-GaN layer. An *x*-polarized dipole was inserted to represent the light emission from MQWs. The simulation range is 30 μm × 30 μm × 7 μm with perfectly matched layer (PML) boundaries in all directions. Two monitors were added to characterize the cross-sectional and top views of the electric field distribution. Either the near-field propagation or the far-field distribution is calculated with an additional script.

The normalized intensity distribution of the electric field in the *x*-*z* plane is shown in the first column of Fig. 4 with different deflection angles. It is evident that the wavefront changes from a curved surface to a planar surface by adding a metalens,

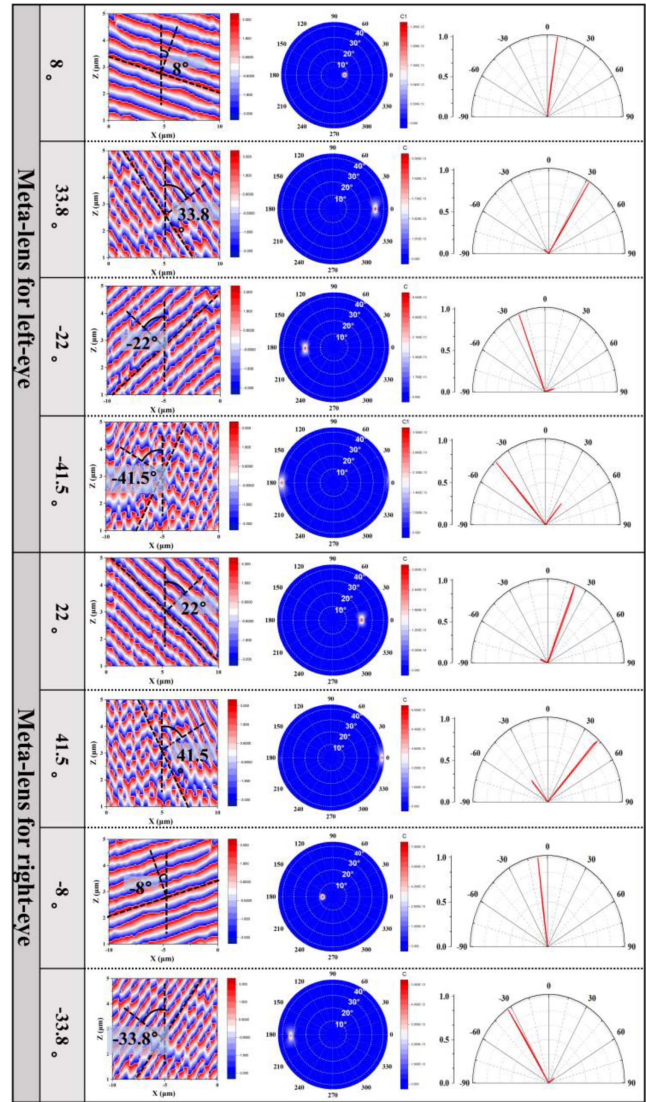


**Fig. 4.** Simulated results of metalens with a specific deflection angle: normalized intensity distribution of electric field in the *x*-*z* plane, normalized far-field light intensity distribution, and their vertical cross section.

demonstrating efficient collimation. However, the collimated performance of a large deflection angle is not as good as that of a small deflection angle, due to the increased phase shift and reduced selective structures in a  $2\pi$  period. The deflection performance can also be demonstrated by the *x*-*z* plane electric field distribution, since the propagation direction is perpendicular to the equal phase plane. The simulated deflection angle matches well with the target one. The normalized far-field light intensity distribution and its vertical cross section are illustrated in the second and third columns of Fig. 4, further confirming the good collimation and deflection effects of the metalens.

To quantify the deflection efficiency, a defined parameter  $\eta_{\text{def}} = I_{\text{def}}/I_{\text{in}}$  is calculated and shown in Table 1, where  $I_{\text{def}}$  is the integrated light intensity within 20° around the target deflection angle and  $I_{\text{in}}$  is the total light intensity emitted from

**Table 1.** Simulated Results of Metalens with a Specific Deflection Angle for Different Viewing Points.

	Metalens for left eye				Metalens for right eye			
	View 1	View 3	View 5	View 7	View 2	View 4	View 6	View 8
Deflection angle (°)	-41.5	-22	8	33.8	-33.8	-8	22	41.5
Position at observation screen (mm)	-223.65	-98.25	33.16	163.34	-163.33	-33.17	98.25	223.65
Deflection efficiency	67.42%	60.65%	91.04%	83.81%	80.19%	91.83%	64.84%	71.36%

the dipole. The results show that the deflection efficiencies for 8° and 22° are over 80%, which dramatically decreases as the deflection angle increases. The deflection efficiency for the large angle can be further improved by reducing the period size.

### 3.2. Metalens for multiple viewing points based on compound eye structure

Double-functioned metalenses with specific deflection angles are demonstrated in Sec. 3.1. However, single deflection is not enough for a large viewing angle, and the increase of the viewing angle is at the expense of resolution and integration. To solve the contradiction between large viewing angle and high resolution, a compound eye structure was introduced to obtain an integrated multiple deflective metalens. The metalens modules with specific deflection angles are spliced and penetrated together, resulting in a multideflection of 8°, 33.8°, -41.5°, and -22° for subpixel 1, and -33.8°, -8°, 22°, and 41.5° for subpixel 2, respectively.

In the design of module splicing, metalens modules with different deflection angles are assembled and arranged from left to right. Each metalens module is cut and spliced within the same coordinate system, with an equivalent area of 15 μm × 30 μm at first. The normalized far-field light intensity distribution and its vertical cross section are simulated for the designed splicing metalens. Figure 5(b) illustrates the multiple deflection angles, with an extremely high deflection intensity at 8° and several impure peaks.

To improve the uniformity of the deflection intensity for different viewing points, the size of each module was carefully adjusted. Table 2 shows the detailed design parameters of the module size for the splicing metalens before and after area ratio adjustment. The intensity will be reduced if the area of the module is reduced. Therefore, we reduced the area of the module for angles of ±22° from 15 μm × 30 μm to 10 μm × 30 μm and reduced the area of ±8° from 15 μm × 30 μm to 9 μm × 30 μm. Figure 5(c) shows the simulated results of the adjusted structure. It is obvious that the uniformity of the deflection intensity is significantly improved. The deflection efficiency of individual angle and the total deflection efficiency are also calculated and are listed in Table 2. The results demonstrate that the total deflection efficiency exceeds 80%. The pixel size of the optical system with the adjusted splicing metalens is 51 μm × 30 μm, and the resolution is 602 PPI (pixels per inch).

In order to further reduce the pixel size and improve the resolution, we propose a metalens design with module penetration, where the unit cells constituting the metalens with two different deflection angles are interspersed. Figure 5(d) shows the schematic diagram of the module penetration. Four deflection angles are separately obtained through two adjacent penetrated modules. The detailed design parameters of the modules for the penetration metalens are given in Table 3. Module 1 is the metalens with deflection angles of ±22° penetrated in a metalens with

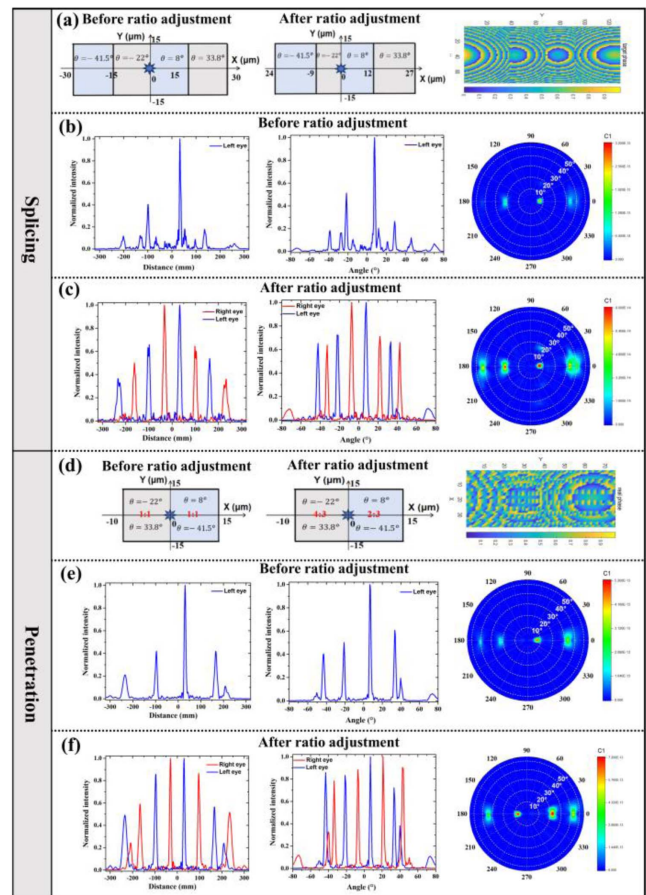


**Fig. 5.** Schematic diagram of (a) module splicing and module penetration metalens; simulation results of module splicing metalens (b) before ratio adjustment and (c) after ratio adjustment; simulation results of module penetration metalens (e) before ratio adjustment and (f) after ratio adjustment.

**Table 2.** Design Parameters and Simulated Results of Multideflected Metalens by Module Splicing.

Deflection angle (°)		Metalens for left eye				Metalens for right eye			
		8°	-22°	33.8°	-41.5°	-8°	22°	-33.8°	41.5°
Splicing (before ratio adjustment)	Area of meta-lens modules ( $\mu\text{m} \times \mu\text{m}$ )	15 × 30	15 × 30	15 × 30	15 × 30	15 × 30	15 × 30	15 × 30	15 × 30
	Deflection efficiency	28%	16.46%	8.88%	6.19%	27.56%	15.95%	8.96%	6.06%
	Total deflection efficiency	59.53%				58.53%			
Splicing (after ratio adjustment)	Area of metalens modules ( $\mu\text{m} \times \mu\text{m}$ )	9 × 30	9 × 30	12 × 30	15 × 30	9 × 30	12 × 30	15 × 30	15 × 30
	Deflection efficiency	18.56%	19.38%	17.05%	21.33%	17.49%	17.49%	23.09%	16.18%
	Total deflection efficiency	76.32%				75.81%			

**Table 3.** Design Parameters and Simulated Results of Multideflected Metalens by Module Penetration.

Deflection angle (°)		Metalens for left eye				Metalens for right eye			
		Module 1		Module 2		Module 1		Module 2	
		-22°	33.8°	8°	-41.5°	-8°	41.5°	22°	-33.8°
Penetration (before ratio adjustment)	Area of metalens modules ( $\mu\text{m} \times \mu\text{m}$ )	15 × 30		15 × 30		15 × 30		15 × 30	
	Quantitative proportion of unit cells	1:1		1:1		1:1		1:1	
	Deflection efficiency	15.95%	19.04%	30.8%	13.33%	29.86%	12.78%	16.06%	19.34%
	Total deflection efficiency	79.12%				78.04%			
Penetration (after ratio adjustment)	Area of metalens modules ( $\mu\text{m} \times \mu\text{m}$ )	15 × 30		15 × 30		15 × 30		15 × 30	
	Quantitative proportion of unit cells	4:3		2:3		2:3		4:3	
	Deflection efficiency	19.38%	17.05%	18.56%	21.33%	17.49%	16.18%	17.49%	23.09%
	Total deflection efficiency	76.32%				75.81%			

deflection angles of  $\pm 33.8^\circ$ , while module 2 is the metalens with deflection angles of  $\pm 8^\circ$  penetrated into deflection angles of  $\pm 41.5^\circ$ . The size of module 1 is  $10 \mu\text{m} \times 30 \mu\text{m}$ , while the size of module 2 is  $15 \mu\text{m} \times 30 \mu\text{m}$ . Each module contains an equal number of unit cells for different angles. The normalized far-field light intensity distribution and its vertical cross section are simulated for the designed penetration metalens. Figure 5(e) illustrates multiple deflection angles, with the deflection intensity at  $8^\circ$  being twice as high as for other deflection angles.

To improve the uniformity of the deflection intensity for different viewing points, the proportion of the penetrated unit cells for different angles is carefully adjusted. Table 3 shows the detailed design parameters of the module size for the penetrated metalens before and after area ratio adjustment. The intensity will be reduced if the number of unit cells is reduced. Therefore, we reduce the ratio of the unit cells for angles of  $\pm 8^\circ$  and  $\pm 41.5^\circ$  from 1:1 to 2:3 under a constant area. Additionally, the ratio of unit cells for angles of  $\pm 22^\circ$  and  $\pm 33.8^\circ$  is also

adjusted from 1:1 to 4:3, contributing to an enhancement of the intensity of angles of  $\pm 22^\circ$ . Figure 5(f) shows the simulated results of the adjusted structure. The uniformity of the deflection intensity is significantly improved. The deflection efficiency of individual angle and the total deflection efficiency are all calculated and listed in Table 3. The results demonstrate that the total deflection efficiency approaches 75%, which is smaller than the spliced metalens. However, the pixel size is significantly reduced to  $25 \mu\text{m} \times 30 \mu\text{m}$  with a resolution of 910 PPI.

The above results show that either the splicing or the penetration metalens structure can achieve an efficient multiple deflection, resulting in a viewing angle of  $41.5^\circ$  with a PPI of 910. The viewing angle can be further increased by adding metalens modules with larger deflection angles. However, the light source in the previous simulation was represented by an  $x$ -polarized dipole, which was not conformed with the real case. The lighting mechanism of the LED is the spontaneous emission via the recombination of electrons and holes, which can be treated as

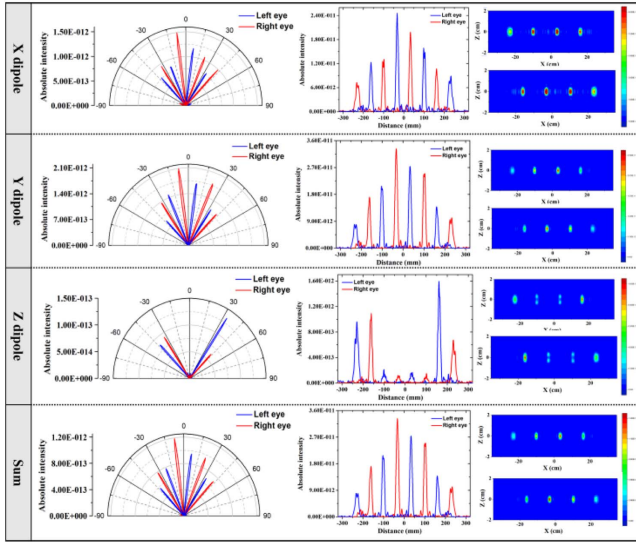


Fig. 6. Calculated far-field intensity distributions with  $x$ -polarized,  $y$ -polarized, and  $z$ -polarized dipoles as well as the average intensities of the incoherent dipoles.

the superposition of electromagnetic point dipole sources. The average electromagnetic field intensity of an ensemble of incoherent, isotropic dipole emitters in a small spatial volume can be calculated by<sup>[25]</sup>

$$|E|^2 = \frac{1}{3}(|E_x|^2 + |E_y|^2 + |E_z|^2), \quad (5)$$

where  $E_x$ ,  $E_y$ , and  $E_z$  are the electromagnetic fields generated by a single dipole along the  $x$ ,  $y$ , and  $z$  axes, respectively. To analyze the performance more accurately, the far-field intensity distribution with  $y$ -polarized and  $z$ -polarized dipoles, as well as the average intensity of the incoherent dipoles, are also calculated, as shown in Fig. 6. The results for the  $x$ -polarized and  $y$ -polarized dipoles are nearly identical, as the unit cells constituting the metalens are symmetric. However, a distinct difference in deflection efficiency is observed with a  $z$ -polarized dipole.

Despite this, the electric field intensity for a  $z$ -polarized dipole is an order of magnitude lower than that for  $x$ - or  $y$ -polarized dipoles. Consequently, the average intensity follows the same trend as that for the  $x$ -polarized dipole, demonstrating efficient multiple deflection.

### 3.3. Dynamically controlled observation position by separating subpixels

To generate a dynamic adjustable observation position, we use  $2N$  subpixels to form one pixel in a 3D display image. To elaborate on the design method and performance of the metalens,  $N = 2$  and  $N = 3$  are selected as examples. For  $N = 2$ , the deflection angles of the metalens for subpixel 1 are  $-41.5^\circ$ ,  $-22^\circ$ ,  $8^\circ$ , and  $33.8^\circ$ ; the angles for subpixel 2 are  $-37.9^\circ$ ,  $-14.6^\circ$ ,  $14.6^\circ$ , and  $37.9^\circ$ ; the angles for subpixel 3 are  $-33.8^\circ$ ,  $-8^\circ$ ,  $22^\circ$ , and  $41.5^\circ$ ; the angles for subpixel 4 are  $-27.5^\circ$ ,  $0^\circ$ , and  $27.5^\circ$ . Table 4 shows the detailed information of the designed metalens for  $N = 2$ . There are eight viewing points when  $OVD = 25$  cm, in which subpixels 1 and 2 show images for the left eye and subpixels 3 and 4 display images for the right eye. There are 15 viewing points when  $OVD = 50$  cm, in which subpixels 1, 2, 3, and 4 are alternately arranged for the left and right eyes. Figure 7(a) demonstrates the far-field luminous intensity distribution of the designed metalens/micro-LED optical systems with  $N = 2$ . The results show a high deflection efficiency of the designed metalens, with negligible cross talk at different viewing points and distances. The light intensity at the middle point is higher than the viewing point with a larger viewing angle, which is beneficial to improve the utilization efficiency at the central view.

For  $N = 3$ , 6 subpixels join into one pixel in 3D display. There are eight viewing points when  $OVD = 25$  cm, in which subpixels 1, 2, and 3 show images for the left eye and subpixels 4, 5, and 6 display images for the right eye. There are 22 viewing points when  $OVD = 75$  cm, in which subpixels 1, 2, 3, 4, 5, and 6 are alternately arranged for the left and right eyes. Figure 7(b) demonstrates the far-field luminous intensity distribution of the designed metalens/micro-LED optical systems with  $N = 3$ . The deflection intensity remains high, but it shows more

Table 4. Design Parameters and Simulated Results of Multideflected Metalens with  $N = 2$ .

	Metalens for subpixel 1				Metalens for subpixel 2				Metalens for subpixel 3				Metalens for subpixel 4			
Deflection angle [°]	-41.5	-22	8	33.8	-37.9	-14.6	14.6	37.9	-33.8	-8	22	41.5	-27.5	0	27.5	
Position at OVD = 25 cm (mm)	-223	-98	33	163	-195	-65	65	195	-163	-33	98	223	-130	0	130	
Viewing point	1(L)	5(L)	9(L)	13(L)	2(L)	6(L)	10(L)	14(L)	3(R)	7(R)	11(R)	15(R)	4(R)	8(R)	12(R)	
Position at OVD = 50 cm (mm)	-446	-196	66	326	-390	-130	130	390	-326	-66	196	446	-260	0	260	
Viewing point	1(L)	5(L)	9(L)	13(L)	2(R)	6(R)	10(R)	14(R)	3(L)	7(L)	11(L)	15(L)	4(R)	8(R)	12(R)	
Deflection efficiency (%)	14.0	24.9	32.0	17.0	14.9	30.2	29.5	22.4	16.8	32.4	24.7	14.2	11.9	37.1	10.8	

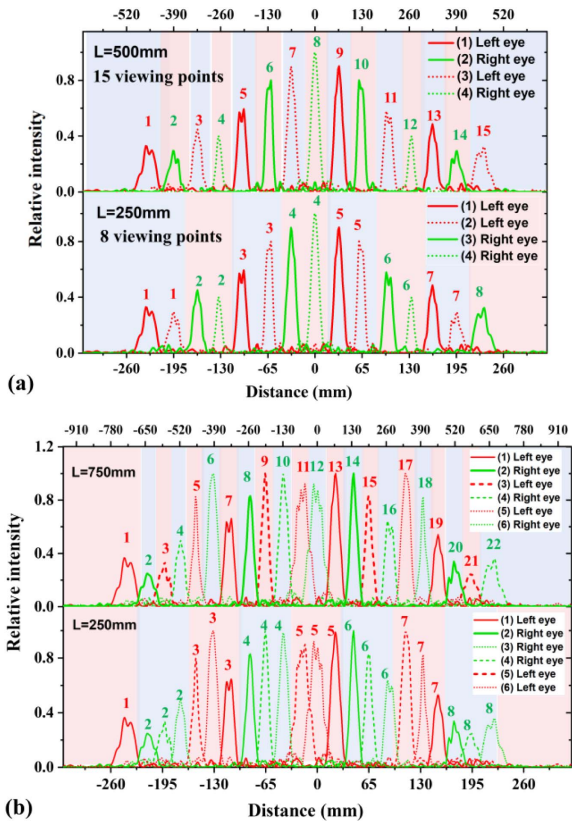


Fig. 7. Far-field luminous intensity distributions of the designed metalens/micro-LED optical systems with (a)  $N = 2$  and (b)  $N = 3$ .

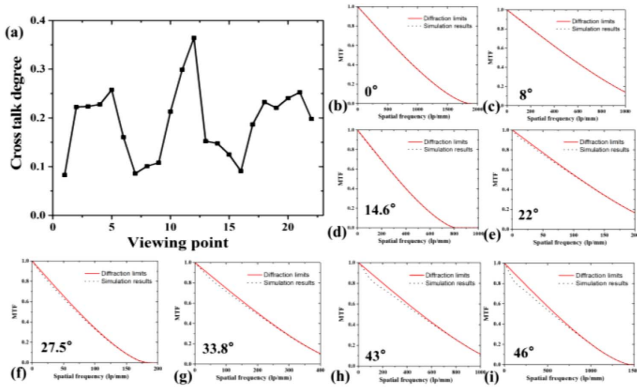


Fig. 8. (a) Calculated cross talk degrees for different viewing points with  $N = 3$  and  $OVD = 75$  cm; (b)–(i) MTF values of the metalens with the same specific deflection angles.

noticeable cross talk between the left-eye and right-eye images, particularly for the central view. The cross talk degree can be quantified using<sup>[26]</sup>

$$\text{crosstalk}(L) = \frac{L_{LKW} + L_{LKK}}{L_{LWK} - L_{LKK}}, \quad \text{crosstalk}(R) = \frac{L_{RWK} + L_{RKK}}{L_{RWK} - L_{RKK}}, \quad (6)$$

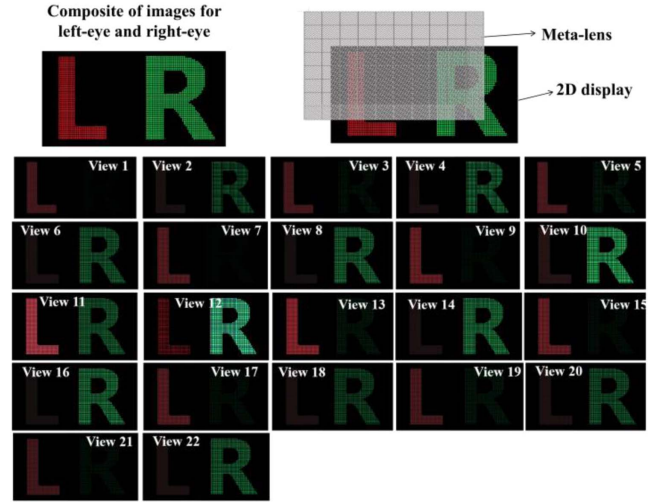


Fig. 9. Calculated images at different viewing points for  $N = 3$  and  $VOD = 75$  cm.

where  $L_{LKW}$  is the intensity at the left view when the subpixels for the left eye are all off,  $L_{LWK}$  is the intensity at the left view when the subpixels for the right eye are all off,  $L_{LKK}$  is the intensity at the left view when all of the subpixels are all off,  $L_{RKW}$  is the intensity at the right view when the subpixels for the right eye are all off,  $L_{RWK}$  is the intensity at the right view when the subpixels for the left eye are all off, and  $L_{RKK}$  is the intensity at the right view when all of the subpixels are all off. Figure 8(a) shows the calculated cross talk degrees for different viewing points. The highest cross talk degree is 0.35.

To evaluate the cross talk effect more visually, we use computer graphic techniques to generate retinal images viewed from various viewing angles with  $N = 3$  and  $OVD = 75$  cm<sup>[27,28]</sup>. The images consist of the letter “L” and the letter “R,” as shown in Fig. 9. It shows obvious cross talk for view 11 and view 12, which can be reduced by further increasing the size of the metalens. In order to further evaluate the overall performance of the optical system, we employ the modulation transfer function (MTF), which quantifies the imaging system’s ability to reproduce contrast at different spatial frequencies<sup>[29,30]</sup>. Higher MTF values indicate better contrast reproduction and sharper images. Figures 8(b) to 8(i) show the MTF values for the metalens with the same specific deflection angles. The MTF value exceeds 0.2 at a spatial frequency of 200 cycles/mm, indicating the capability of the metalens to achieve high-quality eyepiece performance.

#### 4. Conclusion

In summary, we have presented a double-functioned metalens that has functions of collimation and deflection. The FDTD method was employed to simulate the deflection characteristics of the metalens accompanied by the micro-LED. The results of the metalens with a specific deflection angle show an efficient collimation effect and an average deflection efficiency over 80%. The integration of the multiple metalens module by splicing and penetration can result in multiple deflection angles while

maintaining high deflection efficiency and high resolution. The deflection efficiency and resolution are 81%, 602 PPI, and 76%, 910 PPI for the spliced module and the penetration module, respectively. The influence of light polarization on the collimation and deflection performance has also been studied by employing  $x$ -,  $y$ -, and  $z$ -polarized dipoles, respectively. Simulation results demonstrate that the designed metalens is polarization-independent due to the highly symmetric unit structure. Finally, the dynamically controlled observation position has been verified by selected  $N$  values. Our design provides a practical approach for highly integrated micro-LED 3D display based on metalenses.

## Acknowledgements

This work was supported by the National Natural Science Foundation of China (No. 62104187) and the State Key Lab of Digital Manufacturing Equipment & Technology of HUST (No. DMETKF2021014). The SEM work was done at the International Center for Dielectric Research (ICDR), Xi'an Jiaotong University.

## References

1. K. Bang, Y. Jo, M. Chae, *et al.*, "Lenslet VR: thin, flat and wide-FOV virtual reality display using Fresnel lens and Lenslet array," *IEEE Trans. Vis. Comput. Graph.* **27**, 2545 (2021).
2. T. Shu, G. Y. Hu, R. M. Wu, *et al.*, "Compact full-color augmented reality near-eye display using freeform optics and a holographic optical combiner," *Opt. Express* **30**, 31714 (2022).
3. A. Q. Zhang, J. H. Wang, Y. G. Zhou, *et al.*, "Illumination optics in emerging naked-eye 3D display," *Prog. Electromagn. Res.* **159**, 93 (2017).
4. M. F. Schubert and A. M. Hammond, "Fourier modal method for inverse design of metasurface-enhanced micro-LEDs," *Opt. Express* **31**, 42945 (2023).
5. A. R. Anwar, M. T. Sajjad, M. A. Johar, *et al.*, "Recent progress in micro-LED-based display technologies," *Laser Photonics Rev.* **16**, 2100427 (2022).
6. J. E. Ryu, S. Park, Y. Park, *et al.*, "Technological breakthroughs in chip fabrication, transfer, and color conversion for high-performance micro-LED displays," *Adv. Mater.* **35**, 2204947 (2023).
7. P. J. Parbrook, B. Corbett, J. Han, *et al.*, "Micro-light emitting diode: from chips to applications," *Laser Photonics Rev.* **15**, 2000133 (2021).
8. Y. Xing, X. Y. Lin, L. B. Zhang, *et al.*, "Integral imaging-based tabletop light field 3D display with large viewing angle," *Opto-Electron. Adv.* **6**, 220178 (2023).
9. E. L. Hsiang, Z. Y. Yang, Q. Yang, *et al.*, "AR/VR light engines: perspectives and challenges," *Adv. Opt. Photonics* **14**, 783 (2022).
10. Y. Z. Liu, T. W. Xia, A. C. Du, *et al.*, "Omnidirectional color shift suppression of full-color micro-LED displays with enhanced light extraction efficiency," *Opt. Lett.* **48**, 1650 (2023).
11. E. G. Chen, Z. G. Fan, K. X. Zhang, *et al.*, "Broadband beam collimation metasurface for full-color micro-LED displays," *Opt. Express* **32**, 10252 (2024).
12. T. Shu, G. Y. Hu, R. M. Wu, *et al.*, "Compact full-color augmented reality near-eye display using freeform optics and a holographic optical combiner," *Opt. Express* **30**, 31714 (2022).
13. H. S. Park, R. Hoskinson, H. Abdollahi, *et al.*, "Compact near-eye display system using a superlens-based microlens array magnifier," *Opt. Express* **23**, 30618 (2015).
14. S. J. Park, C. Keum, H. Zhou, *et al.*, "Progress and prospects of nanoscale emitter technology for AR/VR displays," *Adv. Mater. Tech.* **8**, 2201070 (2023).
15. L. Zhou, G. L. Bai, X. Guo, *et al.*, "Light beam shaping for collimated emission from white organic light-emitting diodes using customized lenticular microlens arrays structure," *Appl. Phys. Lett.* **112**, 201902 (2018).
16. X. Y. Fu, Y. Mehta, Y. A. Chen, *et al.*, "Directional polarized light emission from thin-film light-emitting diodes," *Adv. Mater.* **33**, 2006801 (2021).
17. E. Khaidarov, Z. T. Liu, R. Paniagua-Dominguez, *et al.*, "Control of LED emission with functional dielectric metasurfaces," *Laser Photon. Rev.* **14**, 1900235 (2020).
18. J. P. Huang, Z. L. Hu, X. Gao, *et al.*, "Unidirectional-emitting GaN-based micro-LED for 3D display," *Opt. Lett.* **46**, 3476 (2021).
19. Y. Xu, J. W. Cui, Z. L. Hu, *et al.*, "Pixel crosstalk in naked-eye micro-LED 3D display," *Appl. Opt.* **60**, 5977 (2021).
20. Y. Meng, Y. Lyu, L. L. Chen, *et al.*, "Motion parallax and lossless resolution autostereoscopic 3D display based on a binocular viewpoint tracking liquid crystal dynamic grating adaptive screen," *Opt. Express* **29**, 35456 (2021).
21. K. H. Yoon, H. Ju, H. Kwon, *et al.*, "Diffraction effects incorporated design of a parallax barrier for a high-density multi-view autostereoscopic 3D display," *Opt. Express* **24**, 4057 (2016).
22. K.-H. Yoon, H. Ju, I. Park, *et al.*, "Determination of the optimum viewing distance for a multi-view auto-stereoscopic 3D display," *Opt. Express* **22**, 22616 (2014).
23. Q. Jiang, G. F. Jin, and L. C. Cao, "When metasurface meets hologram: principle and advances," *Adv. Opt. Photonics* **11**, 518 (2019).
24. S. Yue, Y. X. Liu, R. Wang, *et al.*, "All-silicon polarization-independent broadband achromatic metalens designed for the mid-wave and long-wave infrared," *Opt. Express* **31**, 44340 (2023).
25. Z. H. Tian, M. Y. Zhang, X. Z. Wang, *et al.*, "Simultaneously improve the Purcell factor and internal quantum efficiency of light-emitting diodes via surface plasmon by metal conic structure," *J. Appl. Phys.* **133**, 124901 (2023).
26. X. Zeng, L. Yang, X. Zhou, *et al.*, "Pixel arrangement optimization of two-dimensional light-emitting diode panel for low-crosstalk autostereoscopic light-emitting diode displays," *Opt. Eng.* **56**, 063104 (2017).
27. C. Yao, D. W. Cheng, and Y. T. Wang, "Matrix optics representation and imaging analysis of a light-field near-eye display," *Opt. Express* **28**, 39976 (2020).
28. B. Ye, Y. Fujimoto, T. Sawabe, *et al.*, "A rendering method of microdisplay image to expand pupil movable region without artifacts for lenslet array near-eye displays," in *ICAT-EGVE 2022 Engineering, Computer Science* (2022).
29. Z. B. Fan, Y. F. Cheng, Z. M. Chen, *et al.*, "Integral imaging near-eye 3D display using a nanoimprint metalens array," *Light* **4**, 3 (2024).
30. D. W. Cheng, Y. Liu, C. Yao, *et al.*, "Design of elemental-image-predistortion and splicing seamless integral near-eye display based on aspherical microlens arrays," *Opt. Laser Eng.* **181**, 108365 (2024).